Optics Letters

Channeled spatio-temporal Stokes polarimeters

ISRAEL J. VAUGHN[1], ANDREY S. ALENIN[1], AND J. SCOTT TYO[1]

[1] School of Engineering and IT, University of New South Wales Canberra, Australia
[*] Corresponding author: israel.vaughn@gmail.com

Compiled May 23, 2018

We present the analysis and design of spatio–temporal channeled Stokes polarimeters. We extend our recent work on optimal pixelated polarizer arrays by utilizing temporal carrier generation, resulting in polarimeters that achieve super-resolution via the tradeoff between spatial bandwidth and temporal bandwidth. Utilizing the channel space description, we present a linear-Stokes design and two full-Stokes imaging polarimeter designs that have the potential to operate at the full frame rate of the imaging sensor of the system by using hybrid spatio–temporal carriers. If the objects are not spatially bandlimited, then the achievable temporal bandwidth is more difficult to analyze; however a spatio–temporal tradeoff still exists.

OCIS codes: (100.3010) Image reconstruction techniques, (110.5405) Polarimetric imaging, (120.5410) Polarimetry, (260.5430) Polarization, (120.0280) Remote sensing and sensors

http://dx.doi.org/10.1364/ol.XX.XXXXXX

Two general classes of strategies can be employed in optical polarimeters: 1) divide the light into separate optical paths that are analyzed by independent sets of polarization optics or 2) create a set of harmonic carriers in the analyzer vector amplitude modulated by the scene irradiance distribution.

The measured irradiance in a Stokes polarimeter is

$$s_{0,\text{out}}(\mathbf{x}) = \sum_{j=0}^{3} a_j(\mathbf{x}) \cdot s_{j,\text{obj}}(\mathbf{x}) \tag{1}$$

The parameter set $\mathbf{x}$ represents a set of independent variables such as space [1–3], time [4], angle of incidence [5], etc. where the $a_i's(\mathbf{x})$ generate the carriers. Real instruments take discrete point measurements, and these measurements can be concatenated into a $n \times 1$ vector, $\mathbf{g}_{s_{0,\text{out}}}$. An equivalent expression for Eq. (1) is in the Fourier, or channel domain:

$$S_{0,\text{out}}(\boldsymbol{\rho}) = \sum_{j=0}^{3} A_j(\boldsymbol{\rho}) * \mathbf{S}_j(\boldsymbol{\rho}) \tag{2}$$

where $*$ denotes convolution, $\mathbf{x} \rightarrow \boldsymbol{\rho}$ are the Fourier dual variables, and A_j, S_j are the Fourier transforms of the analyzer and Stokes object functions respectively. In this Letter, we use the spatio-temporal domain $(x, y, t) \rightarrow (\xi, \eta, \nu)$. When the functions a_{mn} are periodic in $\mathbf{x}$, then their Fourier transforms A_{mn} create a 3-dimensional grid of δ-functions in $\boldsymbol{\rho}$. We denote the resultant δ-functions the system's *channels*; the channels are linear and are all added together in the Fourier domain for each Stokes parameter [6]. The linear mixing of each channel at identical channel locations is described by the **Q**-matrix [6].

Previously our group has considered spatio-temporal bandwidth [7–9] and there has been some recent focus by our group and others on spatial or temporal bandwidth alone [3, 4, 10–13]. This work presents a novel spatio-temporal analysis and instrument designs that use Division of Focal Plane (DoFP) polarimeters [2] in combination with one or two retarders and allow spatial and temporal bandwidth to be traded off. We present three novel systems: 1) A linear-Stokes system that has increased bandwidth performance, analogous to super-resolution, over a conventional snapshot system; 2) a full-Stokes system that can reconstruct images at half the temporal bandwidth of the imager; and 3) a full-Stokes system that trades spatial bandwidth for temporal bandwidth. DoFP devices use unit cells of analyzers tiled over a focal plane array (FPA). While several recent studies have shown the value of using more complicated unit cells [2, 3, 10], most systems being manufactured have used 2×2 unit cells. The most common layout is the arrangement of four linearly polarized states shown in Fig. 2A [14], though full-Stokes systems have also been manufactured as shown in Fig. 2B [15]. These systems are "snapshot" polarimeters, in that they can estimate the Stokes parameters at every frame of the image sequence. This is accomplished by giving up some spatial bandwidth [3].

Here we describe systems that use the micropolarizer array (MPA) layouts shown in Figs. 2A and 2C, and couple them with one or two linear retarders. The new systems generate spatio-temporal channels that allow spatial and temporal resolution to be traded off. We begin with the Stokes analyzer description of the MPA in Fig. 2A:

$$\mathbf{a} = \frac{1}{4}\begin{bmatrix} 2 \\ -(\cos\pi x + \cos\pi y) \\ -(\cos\pi x - \cos\pi y) \\ 0 \end{bmatrix}, \tag{3}$$

prior to sampling. A linear-Stokes spatio-temporal system can be constructed by rotating a half waveplate in front of this conventional MPA, denoted CoR. Conceptually, this results in each pixel "rotating" in time with respect to the scene, see visualization 1 which animates the MPA shown in Fig. 2A. Note that Nyquist sampling for the temporal axis is 4 samples per rotation of the half waveplate for this system. We denote the temporal Nyquist sampling rated ν_s. The analyzer vector for the

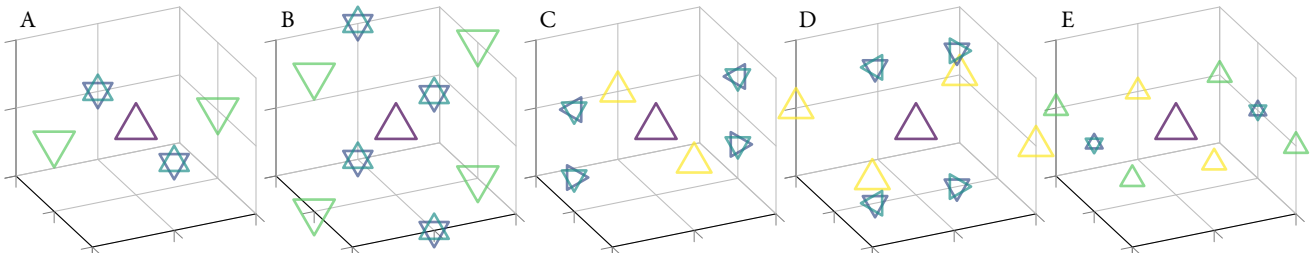

Fig. 1. Channel Structures: (A) Conventional MPA, (B) CoR @ ν_s (C), CoRR @ $2\nu_s$, (D) VATRR @ ν_s, (E) Myhre MPA. The triangles are placed at the channel centers and the area is proportional to the magnitude. Triangles oriented {up, down} and {right, left} represent {positive, negative} real and {positive, negative} imaginary values respectively. The color of each triangle represents the respective Stokes parameter; purple for s_0, dark blue for s_1, turquoise for s_2, and yellow for s_3. The $s_1 + s_2$ channels are annotated in green in (A), (B), and (E).

CoR spatio-temporal system is:

$$\frac{1}{4}\begin{bmatrix} 2 \\ -(\cos\pi x + \cos\pi y)\cos 4\pi\nu_0 T_k \\ -(\cos\pi x - \cos\pi y)\cos 4\pi\nu_0 T_k \\ 0 \end{bmatrix} \tag{4}$$

where $T_k = k/4\nu_0, k \in \mathbb{N}$, and ν_0 is the rotation rate of the half waveplate in rotations per second. If we sample the CoR system at ν_s, we obtain the channel structure shown in Fig. 1B. We graphically represent the channels as complex values in Fig. 1 for the various systems, located at a specific location in the Nyquist cube. The channel structure for the conventional snapshot MPA is shown in Fig. 1A. Notice that the purely temporal bandwidths along lines of ν is the same for both systems at the channel locations, but the spatial channel bandwidth is increased for the CoR system as compared with the conventional system. This result is analogous to the *super-resolution* gained from vibrating color sensors [16]. Given a temporally static scene, multiple snapshots of the same object location are taken that analyze different linear-Stokes states at different time steps. Instead of shaking to obtain the same object location under different spectral pixels as is done in color imaging, we change the polarimetric pixel measurement at the same object location over time.

Two rotating linear retarders can be represented by the Mueller matrix, $\mathbf{RR}(\nu_k, \nu_l, \varepsilon_k, \varepsilon_l; \delta_k, \delta_l)$ [9] where RR_{kl} are elements of $\mathbf{RR}$; ν_k, ν_l are the rotation rates of the first and second retarders respectively; $\varepsilon_k, \varepsilon_l$ are the initial angular offsets of the first and second retarder respectively; and δ_k, δ_l are the retardances of the first and second retarders respectively. See Appendix A in Vaughn [9] for a detailed derivation of dual retarder carrier generation. The rotating retarders can then be combined with a conventional MPA; setting $\delta_k = \pi/2, \delta_l = \pi, \nu_k = \nu_0, \nu_\ell = \nu_0/2, \varepsilon_k = 0, \varepsilon_\ell = -0.03125$, or

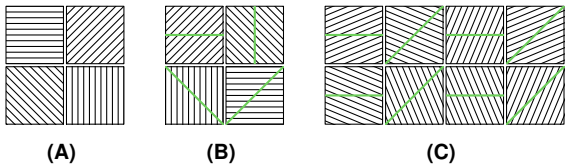

Fig. 2. (A) Conventional MPA. (B) 2×2 Myhre MPA [15] with $\delta = \arccos(1/3)/2$ microretarders. C) This work's 2×4 MPA with $\delta = \pi/2$ microretarders. Pixel hashings and single lines are consistent with the micropolarizer and microretarder orientations respectively.

$\delta_k = \pi, \delta_l = \pi/2, \nu_k = \nu_0, \nu_\ell = 0, \varepsilon_k = 0.03125, \varepsilon_\ell = -0.0625$, where ν_0 is the reference rotation rate, results in

$$\begin{bmatrix} \frac{1}{2} \\ \frac{\sqrt{2}}{8}\cos\pi x\cos 4\pi\nu_0 t \\ \frac{\sqrt{2}}{8}\cos\pi x\sin 4\pi\nu_0 t \\ -\frac{\sqrt{2}}{4}\cos\pi y \end{bmatrix} \text{ or } \begin{bmatrix} \frac{1}{2} \\ \frac{\sqrt{2}}{8}\cos\pi x\sin 4\pi\nu_0 t \\ -\frac{\sqrt{2}}{8}\cos\pi x\cos 4\pi\nu_0 t \\ \frac{\sqrt{2}}{4}\cos\pi y \end{bmatrix} \tag{5}$$

respectively. Taking the 3-D Fourier transform yields 3-D channels with locations on the faces and edges of the Nyquist cube as shown in Fig. 1C. The s_1, s_2 channels are located at $(\pm 1/2, 0, \pm 1/4)$ and the s_3 channels are located at $(0, \pm 1/2, 0)$ when temporally sampled at $2\nu_s$. This channel structure shows that, in the ideal case, if the Stokes parameters images are spatially bandlimited to less than 0.25 cycles per pixel (the same bandwidth limitation of the underlying MPA), then we have twice the temporal bandwidth of a full-Stokes system which uses no spatial carriers [17].

We can formally express an analogous system that is sampled at twice Nyquist in space $(2\xi_s)$ as:

$$\mathbf{a} = \frac{1}{2}\begin{bmatrix} 1 \\ c_1\cos 2\pi x\cos\pi t \\ c_2\cos 2\pi x\sin\pi t \\ c_3\cos\pi x\cos\pi y \end{bmatrix} \tag{6}$$

where c_1, c_2, c_3 are constants determined by the specific system used. We can solve $\mathbf{a} = \mathbf{M}^T\mathbf{p}$ for Eq. (6) where $\mathbf{M}$ is a Mueller matrix [9] and obtain

$$\mathbf{p} = \frac{1}{2}\begin{bmatrix} 1 \\ -\frac{\sqrt{2}}{2}\cos 2\pi x \\ -\frac{\sqrt{2}}{2}\sin 2\pi x \\ \sqrt{2}\cos\pi x\cos\pi y \end{bmatrix}. \tag{7}$$

We can implement such a system by using the novel MPA shown in Fig. 2C and rotating a half waveplate in front of it; we denote this system the Vaughn, Alenin, Tyo rotating retarder (VATRR) system, shown in Fig. 1D. The s_1, s_2 channels are located at $(\pm 1/4, 0, \pm 1/2)$ and the s_3 channels are located at $(\pm 1/2, \pm 1/2, 0)$ when temporally sampled at ν_s. For comparison, the channels of the snapshot full-Stokes system of Myhre, Hsu, Peinado, LaCasse, Brock, Chipman, and Pau are shown in Fig. 1E (Myhre MPA). Each spatio-temporal system has the effect of rotating the lab frame of the microanalyzers of the MPA, generating a temporal carrier on the object at each object pixel location. The spatial carriers taken together with the

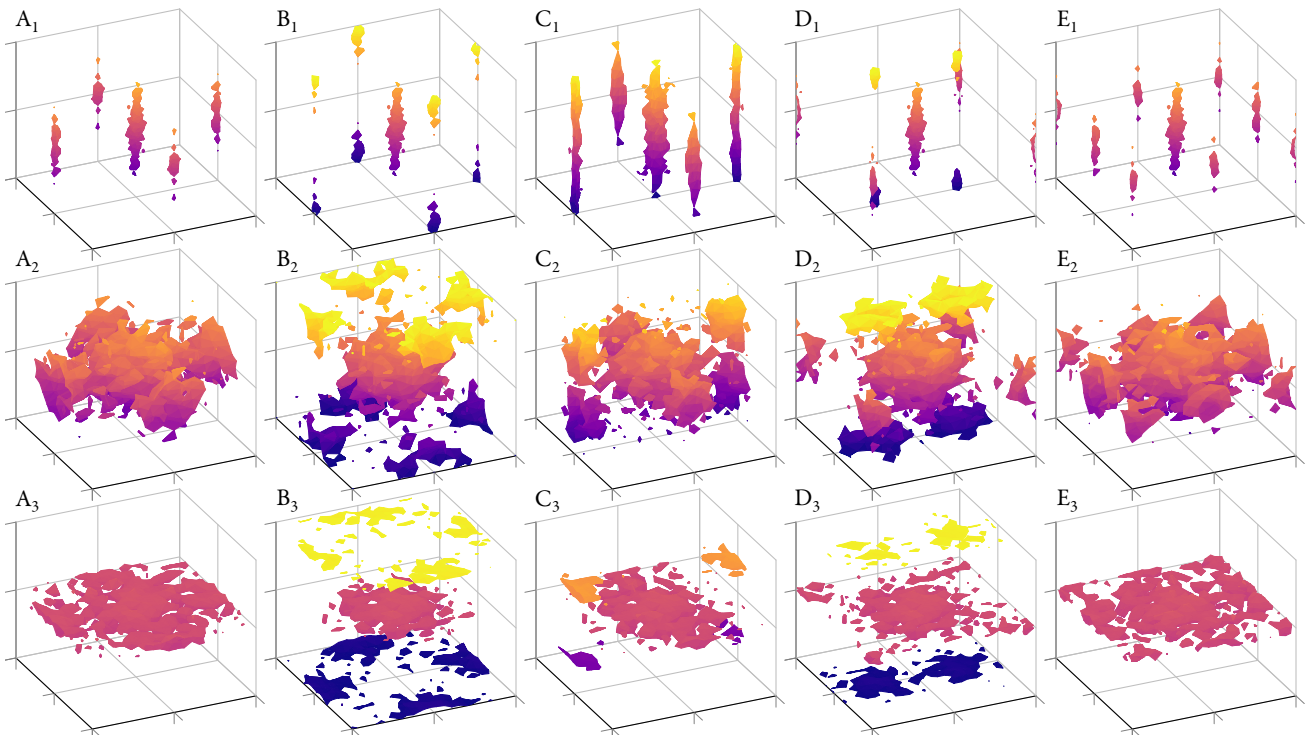

Fig. 3. Isosurfaces of Fourier transform magnitudes: (A) Conventional MPA, (B) CoR @ ν_s (C), CoRR @ $2\nu_s$, (D) VATRR @ ν_s, (E) Myhre MPA. Subscripts denote bandwidth scenarios: (1) low spatial, high temporal, (2) medium spatial, medium temporal, (3) high spatial, low temporal. To aid depth perception, data is colored in accordance with its position along the temporal frequency axis which is mapped into the Cartesian z. Note that the Stokes data is positioned within the Nyquist-cube and is centered around the corresponding channel structures shown in Fig. 1.

temporal carriers generated by the half waveplates generate spatio-temporal carriers.

The full spatio-temporal bandwidth can be determined by looking at the distance between channels in 3-D space, but it is also useful to consider the projection of the sidebands into the spatial frequency plane. In this case, the system is able to produce full-Stokes images at the full temporal resolution of the imager by reducing the spatial bandwidth. The proposed full-Stokes systems in Fig. 1C and 1D are spatio-temporal analogues of one another, with the CoRR system being oversampled in time, and the VATRR system being oversampled in the x-spatial direction. See visualization 2 for the temporal evolution of the CoRR analyzers in the Poincaré sphere, and visualization 3 for the temporal samples of the CoRR system over 2 seconds of elapsed time. Visualizations 4,5 are the temporal animation and temporal samples respectively for the VATRR system.

To characterize the performance of the three new systems, we generate random sets of representative spatio-temporal full- and linear-Stokes data, pass them through a forward instrument model, reconstruct the data cubes, and finally compute the peak signal-to-noise ratio (PSNR) of the reconstructed data. We use a forward model that only relies on the well defined Mueller calculus [17] at each pixel. The retarder parameters specified above and ideal microanalyzer arrays are used. Natural images have power spectral density distributions (PSD) that are proportional to $\approx 0.94/f^{2.073}$ spatially [18]. We generate random spatio-temporal realizations from a $1/f^{3.073}$ distribution and use them for as random object data for the performance analysis, details are in Vaughn, Alenin, and Tyo [19], including the reason for the change in exponent from 2.073 (spatial distributions) to 3.073 (spatio-temporal distributions). The covariance matrix between the Stokes parameters used for the simulation data is specified in prior work [17]. These samples assume natural scenes and natural motion, but may not be representative of other scene types [20] which may contain buildings, edges, etc. Unmixing is accomplished in the Fourier domain [2, 3, 6, 7]. Each system uses an identical 512×512 pixel focal plane array taking 64 frames with identical sampling periods.

We compare the various instruments under the following imaging scenarios 1) a low spatial to temporal bandwidth example, 2) a medium spatial to temporal bandwidth example, and 3) a high spatial to temporal bandwidth example. The system performance of the full-Stokes systems was quantified as follows: 1) sets of 32 image blocks of size $64 \times 64 \times 64$ were generated from the statistical generation algorithms [19], 2) a particle swarm algorithm was used to optimize linear Fourier domain filters for s_0 and the sideband channels separately for each system and each bandwidth type, using the mean PSNR [21] from the 32 image blocks as the cost function, 3) the mean PSNR for

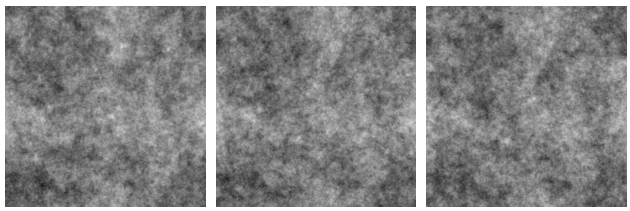

Fig. 4. Sample of the truth s_0 parameter from a PSD with $1/f^{3.073}$ statistics over 3 time steps.

Table 1. Reconstruction PSNR for Various Bandwidth Scenarios[a]

	(A) Conventional MPA		(B) CoR @ ν_s		(C) CoRR @ $2\nu_s$		(D) VATRR @ ν_s		(E) Myhre MPA	
	s_0	DoLP	s_0	DoLP	s_0	DoP	s_0	DoP	s_0	DoP
LSHT	54.8	**36.1**	54.8	35.9	53.4	28.8	50.9	30.8	**53.7**	**34.3**
MSMT	37.2	23.4	**38.9**	**24.2**	38.2	22.9	**38.5**	23.1	37.8	**24.3**
HSLT	40.3	24.5	**56.0**	**28.0**	**45.7**	**31.7**	45.0	27.1	40.7	24.2

[a]LSHT = low spatial, high temporal. MSMT = medium spatial, medium temporal. HSLT = high spatial, low temporal. Values are in dB.

each system was recorded for both systems for each bandwidth type, 4) final datasets were generated and reconstructed using the optimal filters for visualization purposes for the various bandwidth scenarios; see visualizations 6,7 for examples of reconstructed versus truth data for the low spatial to temporal bandwidth example. We can increase the pixel number because the statistical distribution is approximately scale invariant. Fig. 3 shows examples of identical data for the various systems in the Fourier domain for the various bandwidth scenarios. Ideal isosurfaces of each Stokes parameter would be isolated with no crosstalk occurring. Figure 4 shows a sample of the kind of image used for our simulations. Reconstruction results are shown in Table 1.

The CoR system can be implemented by combining a rotating retarder with a conventional MPA. The CoR system performs equally or better than the conventional linear-Stokes snapshot system over all bandwidth scenarios. If the additional instrument complexity can be tolerated, the CoR system will always give higher resolution results than the corresponding snapshot system for linear-Stokes imaging.

If full-Stokes imaging is required, the system must be selected given the specific bandwidth needs of the task at hand. For fast moving scenes a snapshot system should be used. Although we have compared the spatial-temporal systems with the Myhre MPA here, our recent work produced snapshot MPA schemes that outperform the Myhre MPA [12], however the gains are more pronounced for the spatio-temporal systems presented here. For low temporal bandwidth applications, the CoRR system provides an increase in reconstruction performance over the Myhre MPA snapshot and VATRR systems. The system performance is similar between the full-Stokes systems for the medium bandwidth case. The VATRR system, however, provides better high spatial, low temporal bandwidth results than the Myhre MPA, and better DoP results than the CoRR for the low spatial, high temporal bandwidth case. The VATRR system would also perform well when anisotropic spatial bandwidth exists in scenes of interest, e.g. scenes containing a horizon.

Manufacturability is also a concern, the systems that incorporate rotating retarders and conventional linear polarizer arrays (CoR, CoRR) can be manufactured from common off the shelf components (COTS), while the Myhre MPA and the VATRR are a prototype and a design. The VATRR system could be manufactured using techniques similar to the Myhre MPA. As manufacturing ability increases for arbitrary MPAs the potential for novel spatio-temporal designs expands.

In this Letter, we have shown that large bandwidth improvements in polarimetric imaging can be realized via spatio-temporal channeled approaches. The best full-Stokes design depends on the bandwidth statistics of the scenes being imaged; for fast moving, high temporal bandwidth scenes, Myhre's snapshot system outperforms the others, while for high spatial bandwidth, slower moving scenes, the CoRR system is the best performer. The CoRR system is notable due to its ease of implementation using COTS components, resulting in a high performance full-Stokes system. If a range of scenes with low to medium temporal bandwidth is required, then the VATRR system will perform well on average. In an active system where the s_3 component is generally larger, the VATRR system will also perform well given the spatial bandwidth advantage it has over the CoRR and the Myhre MPA systems for the s_3 component. Next steps include analyzing spatio-temporal systems that use *non-separable* carriers [13] (realized by devices like spatial light modulators) to reduce systematic effects [12] and implementing the CoR and CoRR systems in our laboratory.

Funding. Asian Office of Aerospace Research and Development (FA2386-15-1-4098).

REFERENCES

1. M. W. Kudenov, L. Pezzaniti, E. L. Dereniak, and G. R. Gerhart, Opt. Express **16**, 13720 (2008).
2. A. S. Alenin, I. J. Vaughn, and J. S. Tyo, Opt. Lett **42**, 458 (2017).
3. I. J. Vaughn, A. S. Alenin, and J. S. Tyo, Opt. Express **25**, 11954 (2017).
4. C. F. LaCasse, R. A. Chipman, and J. S. Tyo, Opt. Express **19**, 14976 (2011).
5. T. Wakayama, K. Komaki, I. J. Vaughn, J. S. Tyo, Y. Otani, and T. Yoshizawa, Proc. SPIE **8873**, 88730P (2013).
6. A. S. Alenin and J. S. Tyo, J. Opt. Soc. Am. A **31**, 1013 (2014).
7. I. J. Vaughn, O. G. Rodríguez-Herrera, M. Xu, and J. S. Tyo, Proc. SPIE **9613**, 961304 (2015).
8. I. J. Vaughn, O. G. Rodríguez-Herrera, M. Xu, and J. S. Tyo, Proc. SPIE **9613**, 961305 (2015).
9. I. J. Vaughn, , "Bandwidth and noise in spatio-temporally modulated mueller matrix polarimeters," Ph.D. thesis, Uni. of AZ (2016).
10. D. A. LeMaster and K. Hirakawa, Opt. Lett **39**, 1811 (2014).
11. I. J. Vaughn, A. S. Alenin, and J. S. Tyo, Proc. SPIE **9853**, 98530W (2016).
12. A. S. Alenin, I. J. Vaughn, and J. S. Tyo, Applied optics **57**, 2327 (2018).
13. J. Song, I. J. Vaughn, A. S. Alenin, M. E. Gehm, and J. S. Tyo, Proc. SPIE **10655**, 1065517 (2018).
14. C. S. Chun, D. L. Fleming, and E. Torok, Proc. SPIE **2234**, 275 (1994).
15. G. Myhre, W.-L. Hsu, A. Peinado, C. LaCasse, N. Brock, R. A. Chipman, and S. Pau, Opt. Express **20**, 27393 (2012).
16. M. Ben-Ezra, A. Zomet, and S. K. Nayar, IEEE Trans. Pattern Anal. Mach. Intell. **27**, 977 (2005).
17. I. J. Vaughn, A. S. Alenin, and J. S. Tyo, Proc. SPIE **10407**, 1040702 (2017).
18. A. Torralba and A. Oliva, Netw. Comput. Neural Syst. **14**, 391 (2003).
19. I. J. Vaughn, A. S. Alenin, and J. S. Tyo, arXiv preprint arXiv:1707.02723 (2017).
20. R. C. Meredith Kupinski, Proc. SPIE **9853**, 98530P (2016).
21. Z. Wang and A. C. Bovik, IEEE Signal Process Mag **26**, 98 (2009).

FULL REFERENCES

1. M. W. Kudenov, L. Pezzaniti, E. L. Dereniak, and G. R. Gerhart, "Prismatic imaging polarimeter calibration for the infrared spectral region," Opt. Express **16**, 13720–13737 (2008).
2. A. S. Alenin, I. J. Vaughn, and J. S. Tyo, "Optimal bandwidth micropolarizer arrays," Opt. Lett **42**, 458–461 (2017).
3. I. J. Vaughn, A. S. Alenin, and J. S. Tyo, "Focal plane filter array engineering I: rectangular lattices," Opt. Express **25**, 11954–11968 (2017).
4. C. F. LaCasse, R. A. Chipman, and J. S. Tyo, "Band limited data reconstruction in modulated polarimeters," Opt. Express **19**, 14976–14989 (2011).
5. T. Wakayama, K. Komaki, I. J. Vaughn, J. S. Tyo, Y. Otani, and T. Yoshizawa, "Evaluation of mueller matrix of achromatic axially symmetric wave plate," in *SPIE Optical Engineering+ Applications*, vol. 8873 (International Society for Optics and Photonics, 2013), vol. 8873, p. 88730P.
6. A. S. Alenin and J. S. Tyo, "Generalized channeled polarimetry," J. Opt. Soc. Am. A **31**, 1013–1022 (2014).
7. I. J. Vaughn, O. G. Rodríguez-Herrera, M. Xu, and J. S. Tyo, "A portable imaging mueller matrix polarimeter based on a spatio-temporal modulation approach: theory and implementation," (2015), vol. 9613, p. 961304.
8. I. J. Vaughn, O. G. Rodríguez-Herrera, M. Xu, and J. S. Tyo, "Bandwidth and crosstalk considerations in a spatio-temporally modulated polarimeter," (2015), vol. 9613, p. 961305.
9. I. J. Vaughn, "Bandwidth and noise in spatio-temporally modulated mueller matrix polarimeters," Ph.D. thesis, Uni. of AZ (2016).
10. D. A. LeMaster and K. Hirakawa, "Improved microgrid arrangement for integrated imaging polarimeters," Opt. Lett **39**, 1811–1814 (2014).
11. I. J. Vaughn, A. S. Alenin, and J. S. Tyo, "Bounds on the microanalyzer array channel assumption," in *SPIE Commercial + Scientific Sensing and Imaging*, vol. 9853 (International Society for Optics and Photonics, 2016), vol. 9853, p. 98530W.
12. A. S. Alenin, I. J. Vaughn, and J. S. Tyo, "Optimal bandwidth and systematic error of full-stokes micropolarizer arrays," Appl. Opt **(In Review)** (2018).
13. C. S. Chun, D. L. Fleming, and E. Torok, "Polarization-sensitive thermal imaging," in *Automatic Object Recognition IV*, vol. 2234 (International Society for Optics and Photonics, 1994), vol. 2234, pp. 275–287.
14. G. Myhre, W.-L. Hsu, A. Peinado, C. LaCasse, N. Brock, R. A. Chipman, and S. Pau, "Liquid crystal polymer full-stokes division of focal plane polarimeter," Opt. Express **20**, 27393–27409 (2012).
15. M. Ben-Ezra, A. Zomet, and S. K. Nayar, "Video super-resolution using controlled subpixel detector shifts," IEEE Trans. Pattern Anal. Mach. Intell. **27**, 977–987 (2005).
16. I. J. Vaughn, A. S. Alenin, and J. S. Tyo, "A fast stokes polarimeter: preliminary design," in *Polarization Science and Remote Sensing VIII*, vol. 10407 (International Society for Optics and Photonics, 2017), vol. 10407, p. 1040702.
17. A. Torralba and A. Oliva, "Statistics of natural image categories," Netw. Comput. Neural Syst. **14**, 391–412 (2003).
18. I. J. Vaughn, A. S. Alenin, and J. S. Tyo, "Statistical scene generation for polarimetric imaging systems," arXiv preprint arXiv:1707.02723 (2017).
19. R. C. Meredith Kupinski, "Power spectra trends in imaging polarimetry of outdoor solar illuminated scenes," (International Society for Optics and Photonics, 2016), vol. 9853, p. 98530P.
20. Z. Wang and A. C. Bovik, "Mean squared error: Love it or leave it? a new look at signal fidelity measures," IEEE Signal Process Mag **26**, 98–117 (2009).